Marine Geology 336 (2013) 10–23

Contents lists available at SciVerse ScienceDirect

Marine Geology

journal homepage: www.elsevier.com/locate/margeo

# Late Quaternary megaturbidites of the Indus Fan: Origin and stratigraphic significance

J. Bourget [a,*], S. Zaragosi [b], M. Rodriguez [c,d,e], M. Fournier [c,d], T. Garlan [f], N. Chamot-Rooke [e]

[a] Centre for Petroleum Geoscience and $CO_2$ Sequestration, School of Earth and Environment, University of Western Australia, 35 Stirling Hwy, Crawley, WA 6009, Australia
[b] Univ. Bordeaux, EPOC, UMR 5805, F-33400 Talence, France
[c] Institut des Sciences de la Terre de Paris, UMR 7193, Université Pierre et Marie Curie, case 129, place Jussieu, 75252 Paris cedex 05, France
[d] iSTeP, UMR 7193, CNRS, F-75005 Paris, France
[e] Laboratoire de Géologie, Ecole normale supérieure, 24 rue Lhomond, 75231 Paris cedex 05, France
[f] SHOM, Centre Hydrographie, BP146, F-29280 Brest, France

ARTICLE INFO

*Article history:*
Received 9 January 2012
Received in revised form 27 November 2012
Accepted 28 November 2012
Available online 7 December 2012

Communicated by D.J.W. Piper

*Keywords:*
Indus Fan
turbidite system
Quaternary
stratigraphy
sea-level
pull-apart basin
megaturbidite

ABSTRACT

The Indus sedimentary basin forms one of the largest "source-to-sink" systems of the Quaternary and extends over $10^6$ $km^2$ offshore. It is characterized by a complex tectonic setting marked by the Himalayan active orogenic belt in the source area, and the active strike-slip India-Arabia plate boundary (Owen Fracture Zone; OFZ) in its distal reaches. This paper focuses on a Late Quaternary channel–levee system from the Indus Fan captured by the recent opening of the 20°N pull-apart basin, located at 850 km off the present-day Indus Delta, along the OFZ. In this area the channel-mouth deposits consist of a set of up to 23 m thick megaturbidites trapped in the basin. These deposits form "ponded" lobe deposits in a tectonically-active confined basin. Age determination from radiocarbon dating and extrapolation of local deformation rates show that the older deposits observed on the seismic profiles are up to 358 ka BP old (MIS 10). The origin of these Late Quaternary deposits are investigated in the context of the Indus "source-to-sink" system and their significance is placed in a sequence stratigraphic framework. Integration of the stratigraphic architecture of the 20°N Basin megaturbidites with previous work in the area suggests that the Indus Fan evolved from a delta-fed turbidite system with several active canyons and channel–levee during the forced regressive conditions of the last falling stage of sea-level (122–25 ka BP), to a point source turbidite system during the sea-level lowstand (Last Glacial Maximum) and early transgressive stages (25–12 ka BP). This work sheds new light on the recent evolution of the Indus sedimentary system and illustrates the importance of the delta/river evolution during the fall of sea-level (e.g., incised valley formation) on the timing of sedimentary transfer and sediment distribution at the basin-scale.


## 1. Introduction

Large river-fed turbidite systems of the Quaternary (e.g. the Zaire, Amazon, Mississippi, Bengal, Indus, Zambezi or Tanzania deep-sea "fans") develop over distances exceeding 1000 km along continental slopes and abyssal plains (Kolla et al., 1980; Bouma, 1985; Droz and Mougenot, 1987; Kolla and Coumes, 1987; Savoye et al., 2000; Bourget et al., 2008). Intensive mapping of these deep-water giants during the last four decades led to the emergence of detailed architectural (e.g. Normark, 1978; Bouma et al., 1985; Piper and Normark, 2001) and stratigraphic (e.g., Posamentier et al., 1991; Posamentier and Kolla, 2003; Catuneanu et al., 2009) sedimentary models to predict their depositional patterns and their evolution through time. Large mud-rich fans are typically associated with the development of sinuous deep-water channels that extend over several hundreds of kilometers along very low-gradients (Pirmez and Flood, 1995; Peakall et al., 2000). In their distal areas, turbidite systems are associated with the transition between channel/levee systems and sand-rich channel-mouth lobes. On passive-margins, turbidite system growth is generally enhanced when rivers are directly connected to the canyon heads during periods of sea-level lowstands (Vail and Mitchum, 1977; Posamentier et al., 1991; Posamentier and Kolla, 2003; Catuneanu et al., 2009). Conversely periods of sea-level drop (falling-stage) and rise (transgressive) are thought to be dominated by mass-transport deposits and dominantly unconfined flows leading to poor turbidite system development (Posamentier and Kolla, 2003). However, recent studies show that active turbidite system growth in transgression and highstand is possible on tectonically active margins and/or along margins associated with narrow shelves (Goldfinger et al., 2003; Boyd et al., 2008; Bourget et al., 2010; Mas et al., 2010). This has been also observed on passive margins where highstand sediment supply is high enough to by-pass the continental shelves and is transferred basinward, either because of climate-induced high sediment discharges (Ducassou et al., 2009) or maintained river-canyon connection (Khripounoff et al.,

* Corresponding author. Tel.: +61 8 6488 2679.
*E-mail address:* julien.bourget@uwa.edu.au (J. Bourget).

0025-3227/$ – see front matter © 2012 Elsevier B.V. All rights reserved.
http://dx.doi.org/10.1016/j.margeo.2012.11.011

2003). Although the refinement of existing predictive models focusing on the stratigraphic organization of turbidite systems is partly driven by industrial needs, deep-water sedimentary record also constitutes a unique archive of the paleoenvironmental, paleoclimate and tectonic evolution of the source areas. Turbidite systems form the final end-members of the "sediment routing system" and therefore analysis of their stratigraphic evolution can unravel how the sedimentary basin responds to allogenic controls, in a "source-to-sink" perspective.

Here we use geophysical and sedimentary data acquired along the Indian-Arabian plate boundary to illustrate an atypical case of distal deep-water turbidite deposits fed by the Indus turbidite system, one of the largest marine sediment accumulation on earth. The dataset allows investigation of the sedimentary architecture of the 20°N pull-apart basin deposits and their mechanisms of deposition. The results are combined with the pre-existing mapping and dating of the Late Quaternary channel/levee systems from the Indus Fan (Coumes and Kolla, 1984; Kenyon et al., 1995; Prins et al., 2000; Carmichael et al., 2009) in order to examine their origin and their stratigraphic significance. The results highlight the sea-level control on the Late Quaternary evolution of the Indus sedimentary system.

## 2. Regional setting

### 2.1. The Indus turbidite system

The Indus "source-to-sink" system forms one of the most extensive and voluminous sedimentary basin around the world. Indus Fan sedimentation started during the Middle Eocene as the result of the onset of the India-Arabia collision and accelerated since the Early Miocene when uplift of the High Himalayas occurred (Clift et al., 2001, 2002). The Indus River currently drains an area of approximately $1.10^6$ km$^2$ in the Himalayan region, and its annual sediment discharge before damming was about $450.10^6$ T.yr$^{-1}$ (Milliman et al., 1984), representing the fifth largest sediment load in the world. This high sediment load is due to a poorly consolidated sediment source composed of glacial and fluvially-reworked detritus eroded from a high-relief, rapidly uplifting mountain ranges (Milliman et al., 1984; Giosan et al., 2006). Modern water discharge varies seasonally and generally peaks during the summer monsoon season reaching 30,000 m$^3$.s$^{-1}$ (Wells and Coleman, 1984) when the run-off increase due to the combination of snow melting and monsoonal rains (Milliman et al., 1984; Karim and Veizer, 2002). The Indus Delta forms a large sub-aerial delta extending over 750,000 km$^2$ (Fig. 1). The continental shelf develops on an average of 100 km off the present-day delta shoreline, and the shelf-break corresponds to the 135 m isobath (Giosan et al., 2006). Offshore, the Indus turbidite system (referred as "Indus Fan" hereafter) extends over $10^6$ km$^2$ in the Arabian Sea (Fig. 1), reaching 9 km thick at its thickest part (Coumes and Kolla, 1984; McHargue and Webb, 1986; Clift et al., 2001). Glacio-eustatic sea-level changes and subsequent position of the deltaic shoreline are thought to be the main factors that influenced the evolution of the Indus Fan during the Late Quaternary (Kenyon et al., 1995; von Rad and Tahir, 1997; Prins and Postma, 2000; Prins et al., 2000; Bourget et al., 2010). It forms a typical mud-rich, "passive margin fan" (*sensu* Reading and Richards, 1994). The Indus Fan architecture is characterized by numerous high-relief channel/levee systems and channel-mouth lobes (McHargue and Webb, 1986; Kolla and Coumes, 1987; Kenyon et al., 1995; Carmichael et al., 2009) that were fed by several canyon systems (McHargue and Webb, 1986; Kolla and Coumes, 1987). Three canyon complexes have been mapped in the shelf and upper slope areas near the Indus Delta, in an area referred as the Indus Trough (McHargue and Webb, 1986; Kolla and Coumes, 1987). Kolla and Coumes (1987) postulated that the eastern canyon system (Canyon system 3; Fig. 1) was the last active turbidity current pathway and was younger than the western canyon system (Canyon system 2; Fig. 1). However because this early work were based on seismic data and lacked stratigraphic data, the age of both canyon systems remain uncertain. The architectural evolution of the channel–levee systems of the Indus Fan is best constrained during the Late Quaternary and has been unraveled by side-scan sonar mapping and sediment core studies (Kenyon et al., 1995; von Rad and Tahir, 1997; Prins et al., 2000). Two main channel–levee complexes (CLC A and B; Fig. 1) successively formed through avulsion processes during the last sea-level cycle (Kenyon et al., 1995; Prins et al., 2000). The avulsion from CLC B to CLC A occurred at ca. 28 ka BP (Prins et al., 2000), i.e. close to the onset of the Last Glacial Maximum (LGM). The onset of the LGM at about 25 ka BP was characterized by a sea-level dropping from ~60 m to below 120 m in less than 10 ka (Lea et al., 2002; Waelbroeck et al., 2002; Clark et al., 2009). This enhanced rapid incision of the Indus River across the continental shelf, and headward erosion of the Indus Canyon. During the following sea-level lowstand and early rise, which lasted ca. 7500 years, the Indus River sediments were directly funnelled from the fluvial system into the canyon head and promoted the active growth of the CLC A (von Rad and Tahir, 1997; Prins and Postma, 2000; Prins et al., 2000), with reduced if not absent deposition onto the shelf. At present-day, the Indus Canyon is a 185 km long and up to 1.6 km-deep main feeder canyon (Kenyon et al., 1995; von Rad and Tahir, 1997; Prins et al., 2000). The canyon deeply incises the ~100 km-wide continental shelf, with the canyon head being at 20 m water depth, less than 4 km off the present day delta-mouth (Fig. 1). Another canyon system has also been mapped by Kolla and Coumes (1987) to the south-east (Saraswati canyon; Fig. 1). This canyon system would have been fed by the paleo-Saraswati river until the Holocene (Kolla and Coumes, 1987) and could have contributed to the development of the channel–levee complex B during the Late Quaternary (Kenyon et al., 1995).

### 2.2. The Owen Fracture Zone

The 20°N Basin forms a major releasing bend along the Owen Fracture Zone (OFZ) and started to develop about ~1.8–1.5 Ma (Rodriguez et al., 2011). The OFZ is an 800 km-long dextral strike-slip fault which forms the present-day, tectonically-active India-Arabian plate boundary (Fournier et al., 2008, 2011; Rodriguez et al., 2012). The active opening of the 20°N pull-apart basin from the onset of the Pleistocene has been associated with the capture of a distal channel–levee system thought to be part of the Indus Fan (Rodriguez et al., 2011). The present paper focus on the origin, mechanisms of formation and stratigraphic architecture of the 20°N Basin deposits (Fig. 1).

## 3. Material and methods

The bathymetry and acoustic imagery have been collected using the multibeam echosounder Kongsberg-SIMRAD EM120 during the Fanindien 2009 and Owen surveys (*R/V Beautemps-Beaupré*). More than 350 km of sub-bottom seismic profiles (SBP 120 profiler) were also acquired in the 20°N Basin area. Isopach thickness maps between interpreted horizons have been realized with The Kingdom © software. Two-way travel times (TWT) have been converted in m using an average seismic velocity of 1515 m.s$^{-1}$, corresponding to the typical internal acoustic velocity (*P* wave velocity) measured in the cores using a laboratory celerimeter during Fanindien 2009 cruise. Piston cores KS07 (60° 46.65 E; 19° 26.61 N), KS11 (61°18.48 E; 20°10.53 N) and KS12 (61°29.68 E; 20°11.53 N) were collected (using a Küllenberg corer). Thin slabs (15 mm-thick) were sampled and analyzed in the SCOPIX X-ray image processing tool. Grain size analyses were performed using a Malvern™ Supersizer 'S'. Nine AMS $^{14}$C dates have been obtained from mainly bulk planktonic foraminifer species sampled in hemipelagic clay intervals (Table 1). Radiocarbon dates have been corrected for a marine reservoir and calibrated to calendar years using the Calib 6.0.1 calibration program (Stuiver et al., 1998) with the Marine09 radiocarbon calibration curve (Reimer et al., 2009).

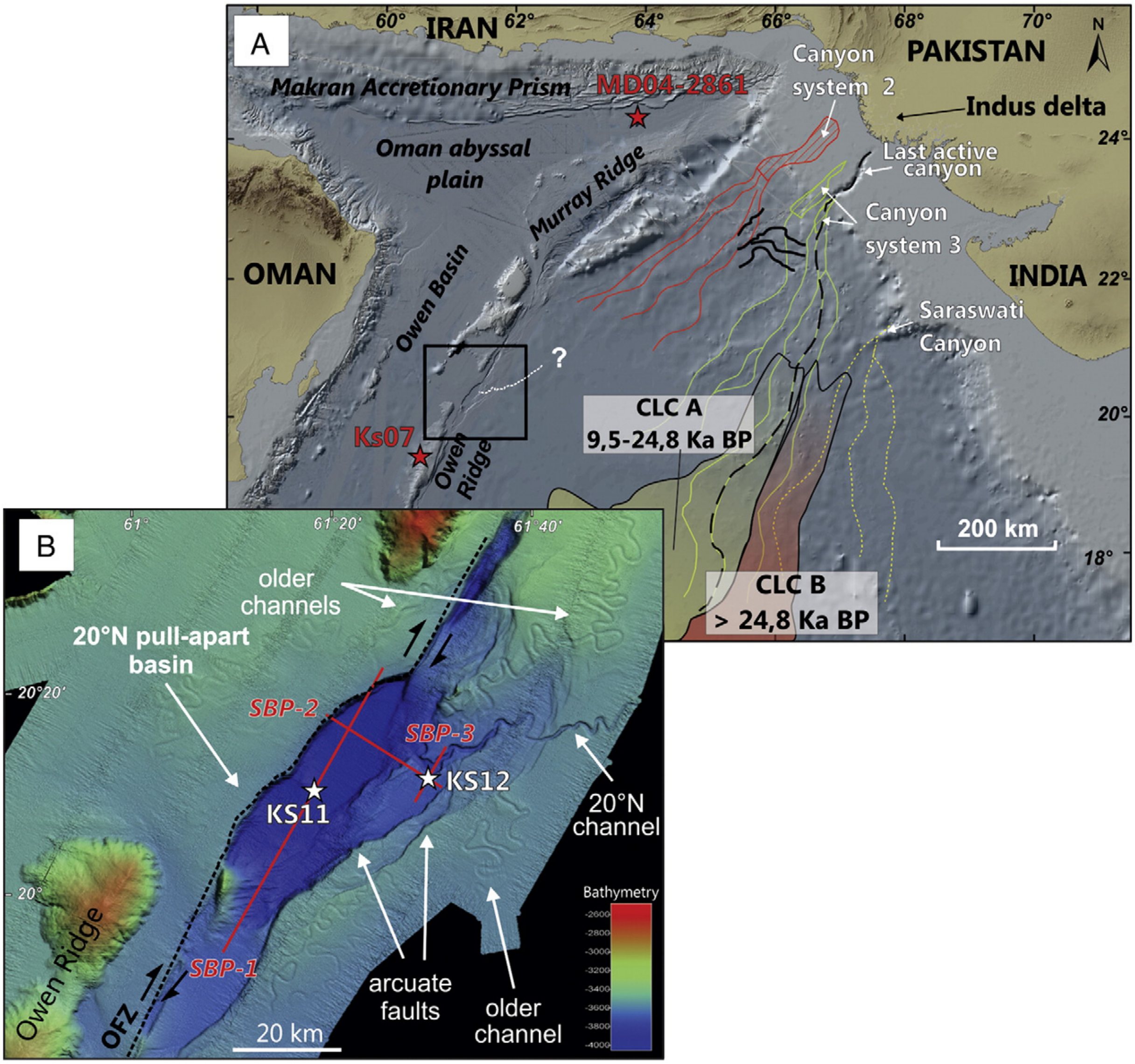


**Fig. 1.** (A) Physiography of the Arabian Sea, location of stratigraphic (hemipelagic) cores KS07 and MD04-2861 (Caley et al., 2011), distribution of Late Quaternary canyons and channel/levee systems of the Indus Fan. Canyon systems 2–3 and the Saraswati Canyon have been mapped by Kolla and Coumes (1987). The last active Indus canyon and the channel–levee complexes A and B were mapped by Kenyon et al. (1995) and Prins et al. (2000). Canyon-channels in black solid lines correspond to the upper Pleistocene Indus canyon/channels of Carmichael et al (2009). Age of the avulsion between CLC A and B is from Prins et al. (2000). (B) Multi-beam bathymetry of the 20°N pull-apart basin along the Owen Fracture Zone (OFZ). Location of the very-high resolution, sub-bottom seismic profiles (SBP-1 to SBP-3) and cores KS11 and KS12.

Radiocarbon ages of this study were performed at the "Laboratoire de Mesure du Carbone 14" in Saclay (SacA) through the "ARTEMIS" radiocarbon dating project. All the ages in the following text are given in calendar age (cal ka BP). Core stratigraphy and correlation have been also based on semi-quantitative geochemical element analyses performed at a cm-scale along the cores using an Avaatech © XRF "Core Scanner". We used the Bromine counts (associated with marine organic content (MOC) in the sediment of Arabian Sea; Ziegler et al., 2008) to correlate the cores KS11, KS12, and KS07 with the MD04-2861 (63° 54.79 E; 24° 7.99 N) stratigraphic reference (Caley et al., 2011). KS07 is located on the Owen Ridge and entirely composed of silt-mud sediments of hemipelagic origin. It therefore constitutes a good local stratigraphic reference that could be correlated to MD04-2861 (Fig. 1). Age model of the core MD04-2861 has been obtained through a combination of radiocarbon dates, biostratiographic correlations and oxygen isotope data (see Caley et al. (2011) for more details). More information about the XRF scanning technique and its relevance in paleo-environmental reconstructions can be found in Richter et al. (2006). Volume calculations of the turbidite events M1–M8 have been obtained through seismic interpretation of horizons across the 20°N Basin and creation of isopach maps using The Kingdom Software© (SMT). However, mapping extrapolation has been limited to a maximum distance of 2 km from the seismic profiles, resulting in a spatial coverage of only 66% of the total 20°N Basin surface. Hence in order to approach a more realistic volume value, estimation of the "total volume" deposited by each event has been calculated by applying a factor 1.5 (Table 2). However, these values are over-estimated as they encompass both turbiditic and hemipelagic deposits. In order to compare the volume of 20°N Basin deposits with previous studies, we therefore applied a correction factor based on the estimation of the proportion of hemipelagic deposits in the centre of the basin. We based our estimation on the depth correlation of the age of the M5 event, located at a maximum of 28 m deep in the basin centre (turbidites + hemipelagites) and corresponding to an age-equivalent depth of 3.5 m on KS07 (hemipelagic deposits only).

**Table 1**
Radiocarbon ages of cores used in this study, including source of the data if previously published.

| Core | Depth in core (cm) | Laboratory code | Material | $^{14}$C age (yr BP) | | | Calendar age (cal yr BP) | Source of data |
|---|---|---|---|---|---|---|---|---|
| MD042861 | 70 | SacA 19505 | Bulk. Pl. form. | 3905 | +/− | 30 | 3877 | Caley et al. (2011) |
| MD042861 | 140 | SacA 19506 | Bulk. Pl. form. | 6900 | +/− | 35 | 7416 | Caley et al. (2011) |
| MD042861 | 250 | SacA 17219 | *G. dutertrei* | 9845 | +/− | 45 | 10,757 | Caley et al. (2011) |
| MD042861 | 250 | SacA 17218 | *G. ruber* | 10,345 | +/− | 45 | 11,325 | Caley et al. (2011) |
| MD042861 | 180 | SacA 17216 | *G. ruber* | 12,170 | +/− | 50 | 13,635 | Caley et al. (2011) |
| MD042861 | 180 | SacA 17217 | *G. dutertrei* | 12,485 | +/− | 50 | 13,922 | Caley et al. (2011) |
| MD042861 | 339.5 | SacA 10439 | Bulk. Pl. form. | 14,160 | +/− | 60 | 16,866 | Bourget et al. (2011) |
| MD042861 | 450 | SacA 17220 | Bulk. Pl. form. | 17,470 | +/− | 70 | 20,268 | Caley et al. (2011) |
| MD042861 | 480 | SacA 22364 | Praeorbulina | 18,290 | +/− | 60 | 21,381 | Caley et al. (2011) |
| MD042861 | 500 | SacA 17221 | Bulk. Pl. form. | 19,850 | +/− | 70 | 23,310 | Caley et al. (2011) |
| MD042861 | 640 | SacA 17222 | Bulk. Pl. form. | 25,170 | +/− | 140 | 29,596 | Caley et al. (2011) |
| MD042861 | 810 | SacA 19507 | Bulk. Pl. form. | 34,170 | +/− | 260 | 38,711 | Caley et al. (2011) |
| KS11 | 178 | SacA 19504 | Bulk. Pl. form. | 18,140 | +/− | 70 | 21,245 | *This study* |
| KS11 | 462.5 | SacA 19499 | Bulk. Pl. form. | 23,850 | +/− | 90 | 28,236 | *This study* |
| KS11 | 512.5 | SacA 19501 | Bulk. Pl. form. | 25,970 | +/− | 130 | 30,409 | *This study* |
| KS11 | 606 | SacA 19503 | Bulk. Pl. form. | 28,480 | +/− | 160 | 32,271 | *This study* |
| KS11 | 733 | SacA 19500 | Bulk. Pl. form. | 31,430 | +/− | 220 | 35,330 | *This study* |
| KS12 | 136.5 | SacA 19502 | Bulk. Pl. form. | 21,750 | +/− | 100 | 25,493 | *This study* |
| KS07 | 0 | SacA 23237 | Bulk. Pl. form. | 2925 | +/− | 30 | 2713 | *This study* |
| KS07 | 20 | SacA 23238 | Bulk. Pl. form. | 8535 | +/− | 30 | 9177 | *This study* |
| KS07 | 40 | SacA 23239 | Bulk. Pl. form. | 12,405 | +/− | 40 | 13,849 | *This study* |
| KS07 | 55 | SacA 21240 | Bulk. Pl. form. | 13,620 | +/− | 50 | 16,209 | *This study* |
| KS07 | 60 | SacA 23240 | Bulk. Pl. form. | 14,710 | +/− | 50 | 17,384 | *This study* |
| KS07 | 150 | SacA 23241 | Bulk. Pl. form. | 20,970 | +/− | 80 | 24,560 | *This study* |
| KS07 | 329 | SacA 23242 | Bulk. Pl. form. | 34,800 | +/− | 290 | 39,292 | *This study* |
| KS07 | 376 | SacA 21241 | Bulk. Pl. form. | 35,130 | +/− | 300 | 39,759 | *This study* |

The latter result suggests that hemipelagic deposits contribute to 12.5% of the total deposit thickness in the basin centre. This factor has been applied to correct the volume calculations in Table 2.

## 4. Results

### 4.1. Sedimentary architecture of the 20°N Basin

The 20°N Basin forms a 90 km long and up to 35 km wide pull-apart basin, however restricted to less than 15 km wide off the mouth of an east-west trending channel–levee system (Figs. 1, 2). The basin is bounded by two major strike-slip faults (Fig. 1) trending N25°E to N30°E (Rodriguez et al., 2011). The western side of the basin is bounded by the OFZ as a steep master fault, and the structural pattern of the eastern basin boundary is more complex and consists of a single normal fault dividing into several arcuate splays (Figs. 2 and 3; Rodriguez et al., 2011). The eastern area is marked by the capture of a 1–3 km wide channel–levee system (Fig. 3). Its trajectory and sinuosity seem to be closely related to the propagation of the SW–NE trending arcuate active faults that are preserved on the bathymetry (Fig. 3). Levees relief varies between 30 and 115 m along the surveyed area and the sections marked by an increase in height correspond to the

**Table 2**
Measured characteristics of M1–M20 megaturbidite beds (thickness on Log Section 1 (S1), maximum thickness (*) measured in the centre of the 20°N basin, volume calculated from seismic interpretation and extrapolation, dip angles at S1 and S2, measured offset in caused by F1 fault) and chronostratigraphy from radiocarbon measurements, oxygen isotope correlation (**) from the core MD04-2861 (Caley et al., 2011), and interpolated ages (see text for explanation). *** Final megaturbidite ages correspond to chronostratigraphy results when available (M1–M9) then are based on extrapolation method (M9–M20). Ages from M14–M20 correspond to the average age obtained from S1 and S2 measurements. Uncertainty in age estimation is obtained from the calculated error in radiocarbon (M1–M5) and radioisotopic dating (M6–M8; Caley et al., 2011), and from the root mean square of the mean statistical variance for M9–M20 (see text for explanation).

| | Thickness S1 (m) | Thickness max. (m) * | Volume (km3) | $^{14}$C age KS11/KS12 | MD-61 age model** | Dip S1 (°) | Fault offset S1 (m) | Interpolated age S1 | Dip S2 (°) | Interpolated age S2 | Megaturbidites age *** | Uncertainty (yr) |
|---|---|---|---|---|---|---|---|---|---|---|---|---|
| Sea-floor | – | – | – | *0* | *0* | 0.190 | 3.540 | – | – | – | – | |
| M1 | 1.9 | 5.9 | 1.03 | *21,245* | – | 0.270 | 4.744 | – | – | – | *21,245* | *<260* |
| M2 | – | 1.3 | – | *25,155* | – | | – | – | – | – | *25,155* | *<260* |
| M3 | – | 1.5 | 0.40 | *28,237* | *29,597* | 0.280 | 6.390 | – | – | – | *28,237* | *<260* |
| M4 | 2.6 | 6.9 | 1.48 | *32,271* | – | 0.330 | 8.701 | – | – | – | *32,271* | *<260* |
| M5 | 4.7 | 8.0 | 1.87 | *35,331* | *38,711* | 0.380 | 9.837 | – | – | – | *35,331* | *<260* |
| M6 | 2.3 | 6.4 | 1.29 | – | *64,000* | 0.440 | 11.879 | – | – | – | *64,000* | *<1000* |
| M7 | 7.7 | 11.3 | 2.79 | – | *74,000* | 0.480 | 12.518 | – | – | – | *74,000* | *<1000* |
| M8 | 4.7 | 7.2 | 1.95 | – | *85,000* | 0.540 | 14.560 | – | – | – | *85,000* | *<1000* |
| M9 | 15.0 | 20.7 | – | – | – | 0.580 | 15.128 | *96,625* | – | – | *96,625* | *10,000* |
| M10 | 18.8 | 23.7 | – | – | – | 0.660 | – | *116,625* | – | – | *116,625* | *10,000* |
| M11 | 3.5 | 3.8 | – | – | – | 0.720 | – | *131,625* | – | – | *131,625* | *10,000* |
| M12 | 3.0 | 3.2 | – | – | – | 0.790 | – | *149,125* | – | – | *149,125* | *10,000* |
| M13 | 2.6 | 3.9 | – | – | – | 0.890 | – | *174,125* | – | – | *174,125* | *10,000* |
| M14 | 0.9 | – | – | – | – | 0.930 | – | *184,125* | 0.390 | *196,369* | *190,247* | *10,000* |
| M15 | 7.5 | – | – | – | – | 1.050 | – | *214,125* | 0.398 | *203,667* | *208,896* | *10,000* |
| M16 | 7.5 | – | – | – | – | 1.100 | – | *226,625* | 0.400 | *205,752* | *216,189* | *10,000* |
| M17 | 8.2 | – | – | – | – | 1.140 | – | *236,625* | 0.423 | *229,557* | *233,091* | *10,000* |
| M18 | 7.3 | – | – | – | – | 1.250 | – | *264,125* | 0.452 | *257,881* | *261,003* | *10,000* |
| M19 | 5.6 | – | – | – | – | 1.290 | – | *274,125* | 0.474 | *280,296* | *277,211* | *10,000* |
| M20 | 31.2 | – | – | – | – | – | – | – | 0.552 | *357,794* | *357,794* | *49,000* |

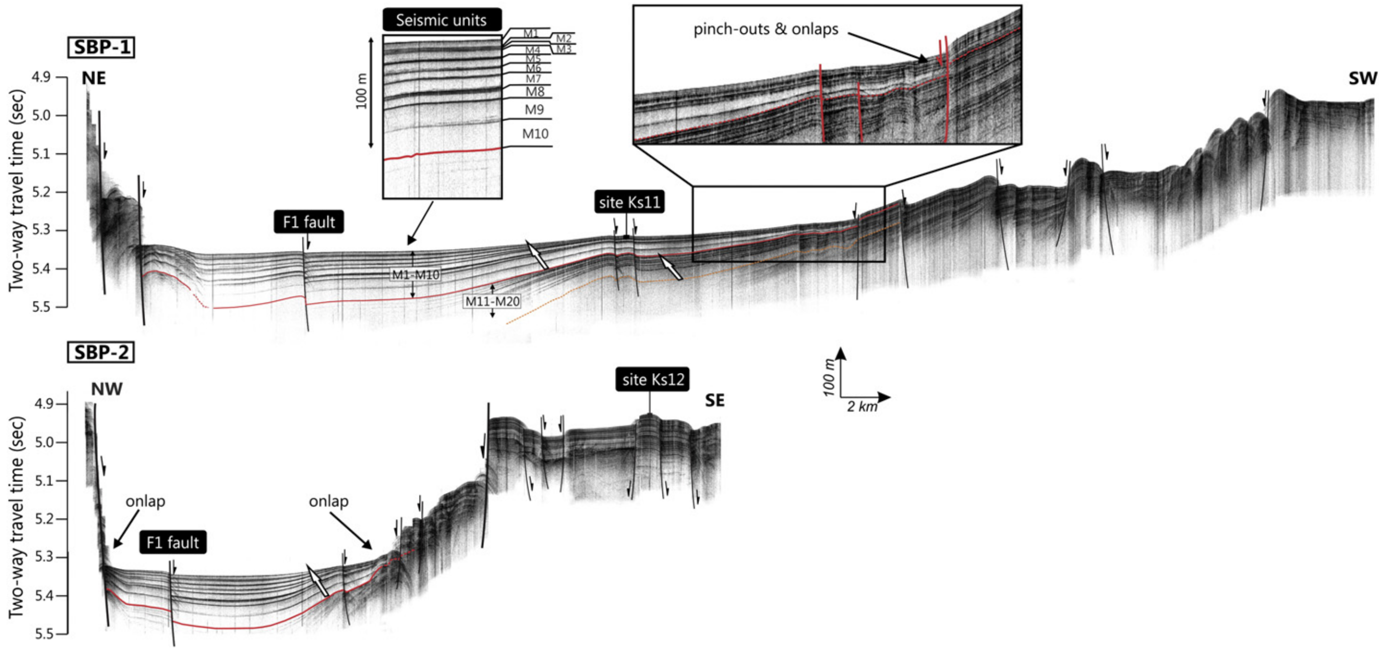


**Fig. 2.** Sub-bottom seismic profiles SBP-1 and SBP-2 (see location on Fig. 1) showing the internal architecture of the 20°N Basin deposits and the megaturbidites M1–M20. White arrows indicate thinning-upward sedimentary sequences.

locations where fault-induced knickpoint cause channel entrenchment. The channel course abruptly terminates into the 20°N Basin where a system of normal faults form a > 120 m high knickpoint (Fig. 3) associated with an abrupt increase of slope gradient (from <1° to 3–5°). Lower relief sinuous channels are also observed within the study area and correspond to older, partly buried channel–levee systems (Fig. 3; Rodriguez et al., 2011). These channels are thought to be inactive since 1.32–0.95 Ma BP (Rodriguez et al., 2011). The edges of the 20°N Basin are generally sharp and despite the fact that its walls have slopes of 10–30° (particularly along its western edge), major slump scars are neither observed along the high-resolution bathymetry (Figs. 1, 3) nor on seismic profiles (Fig. 2). The basin fill is characterized by a vertical stacking of seismic units showing a dominant transparent acoustic echo-facies (Figs. 2, 4). These units considerably thicken in the centre of the basin where they reach more than 0.033 s TWT thick, i.e. up to 25 m (M10, Figs. 2, 4). The seismic units are associated with pinch-out geometry on the edges of the basin in both S–N and E–W directions (Fig. 2), where individual seismic units become considerably thinner (~70% thinner at site KS11, and about 95% twenty kilometers to the north on line SbP-2). The base of the seismic units is often characterized by higher seismic amplitudes (Figs. 2, 4). Twenty seismic units (named M1 to M20 hereafter) have been consistently recognized in the 20°N Basin (Figs. 2, 4). Below M20, sub-bottom profiler penetration decreases and interpretation is difficult. The vertical distribution of seismic units allows differentiating two thinning-upward sedimentary intervals (Figs. 2, 4). The upper ten seismic units (M1–M10) form a max. 0.132 s. TWT thick sequence in the center of the basin, i.e., about 100 m (Figs. 2, 4). Thickness of individual seismic units measured on Section 1 (Fig. 4) decreases from M10 (18.8 m thick) to M1 (1.9 m thick; Table 2). Seismic units M11 to M20 form a second thinning-upward sequence with a maximum thickness of 64 m on Section 1 (Fig. 4), and individual seismic units ranging from 31.2 m (M20) to 3.5 m thick (M11; Table 2). Although some seismic profiles suggest that this second thinning-upward sequence also includes deeper seismic units (Figs. 2, 4), these cannot be consistently mapped over the area and therefore are not considered in the following discussion. The 20°N Basin deposits are perturbed by a transverse fault system (F1) that offsets the M1–M20 seismic units in the north-western area (Fig. 4). It causes an offset of 3.5 to 16.3 m in the seismic units along the two measured sections shown in Fig. 4, the offset decreasing from the deeper seismic units (M9) to the shallower (M1; Table 2). Below M9 the fault offset cannot be calculated due to the lack of acoustic penetration in seismic profiles in the F1 fault area (Figs. 2, 4).

### 4.2. Sedimentary cores

Cores KS11 and KS12 were recovered on the southwestern edge of the 20°N Basin and on the left-hand levee of the channel–levee system, respectively (Fig. 1). Both cores are composed of fine-grained sediments, mostly clay to silty clay-sized particles (Fig. 5). Coarse silt layers are observed throughout the cores ($D_{50}$ = 11–40 μm; Figs. 5, 6). In both KS11 and KS12 they form thin (mm to dm-thick), fining-upward layers commonly associated with planar lamination, possible convolute bedding, and slightly erosional bases (Fig. 6). These coarse to fine silt layers grade up to structureless clays ($D_{50}$ = 4–11 μm). The upper, muddy unit is generally bioturbated and has variable planktonic foraminifer content. Thus, KS11 and KS12 deposits can be interpreted as fine-grained turbidites ("Tc "or "Td" of Bouma, 1962) capped by turbiditic muds ("Te") and hemipelagic sediments. Combination of AMS-$^{14}$C dating and XRF records enables correlations between the two cores (Fig. 5). Their Bromine (Br) record could also be correlated with cores KS07 and MD04-2861 (Fig. 1). These two cores are composed of hemipelagic sediments and are located away from any turbiditic input (Fig. 1; Caley et al., 2011). MD04-2861 is a regional stratigraphic reference providing a complete record of the paleo-environmental evolution of the Arabian Sea during the last 310 ka BP (Caley et al., 2011). Stratigraphic data show that turbidite activity in the 20°N Basin ceased after 25.4 and 21.2 ka BP at sites KS12 and KS11, respectively (Fig. 5), an age which roughly corresponds to the onset of the Last Glacial Maximum (LGM).

### 4.3. Nature and age of the 20°N Basin deposits

#### 4.3.1. Seismic-core correlation

As the seismic units pinch-out toward the edges of the basin (Fig. 2), the 9 m-long core KS11 potentially recovered much of the thick sedimentary succession in the centre of the 20°N Basin. Sand

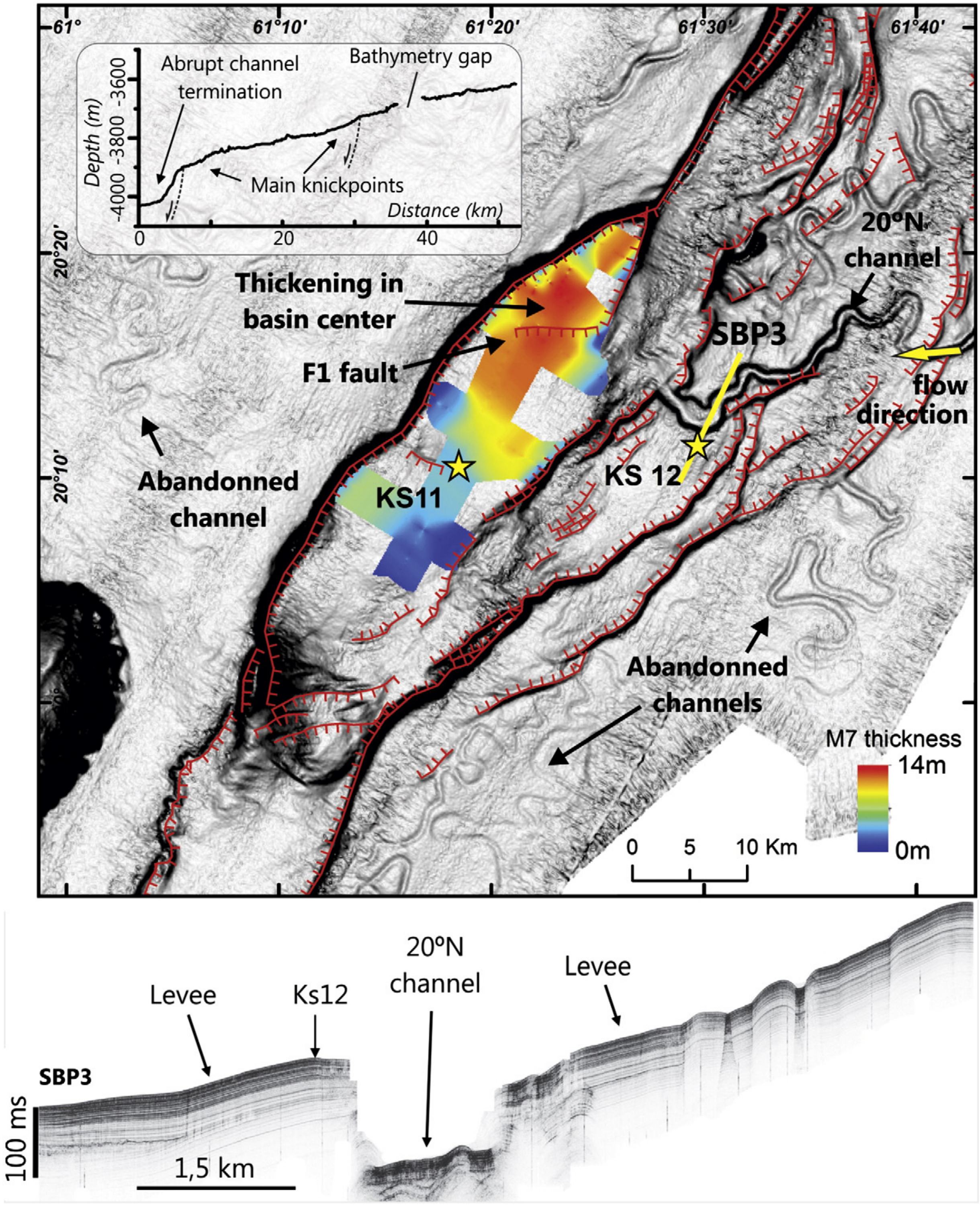


**Fig. 3.** Slope map of the 20°N Basin showing the distribution of the main structural elements (brown lines), the location of the cores KS11 and KS12, the last active Indus channel and the abandoned Indus channels (Rodriguez et al., 2011). SBP-3 sub-bottom seismic profile shows a cross-section of the last active Indus channel before it enters the 20°N Basin. Along-channel bathymetry profile highlights the location of main slope breaks along the last active Indus channel pathway including the >100 m high knickpoint at the 20°N Basin eastern edge. Thickness map of the megaturbidite M7 highlights megaturbidite deposition thickening in the basin centre and thinning on basin edges.

to silt turbidite bases typically produce strong contrast of impedance on sub-bottom, high-frequency seismic (Cita and Rimoldi, 1997; Rothwell et al., 2000). The key reflectors observed in the first 10 meters depth on seismic profiles at site KS11 can be correlated with the sand to silt turbidite bases observed in the core using a seismic velocity of 1515 m.s$^{-1}$ (Fig. 6). These reflectors define the base of the thick seismic units M1 to M5 observed in the centre of the basin centre (Fig. 6). Hence M1 to M5 units form a total thickness of about 26 m in the basin centre, corresponding to less than 9 m thick at site KS11 (Fig. 6). Older deposits (M6–20) are not recovered in KS11 (Figs. 5, 6) but show an acoustic facies similar to the M1–5 events, consisting of a thin high to moderate amplitude base capped by a thick transparent

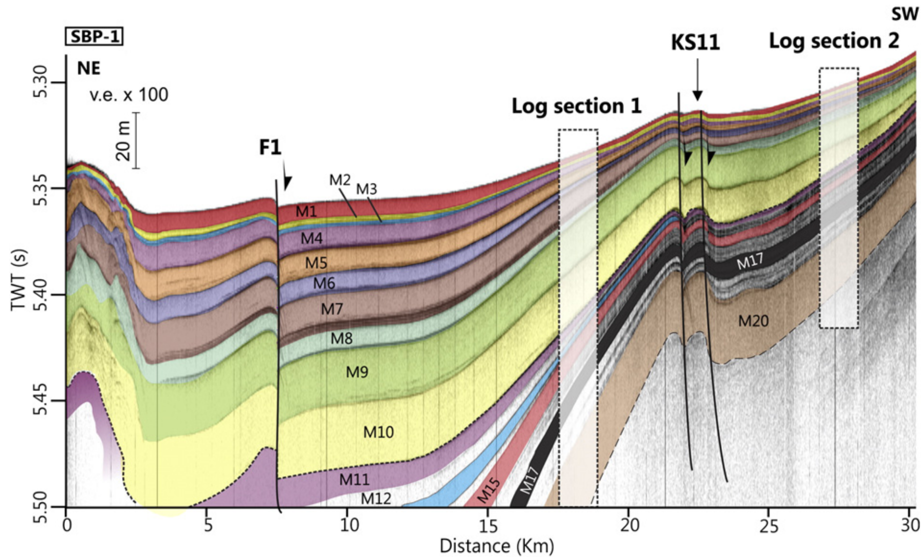


**Fig. 4.** Interpreted seismic profile SBP-1 showing the architecture of M20–M1 deposits, their offset at F1 fault location, and the location of log Sections 1 and 2 where dip angles have been measured.

echo-facies (Figs. 2, 4, 6). We interpret the basal strong reflections to be produced by sand to silt turbidite bases, which thicken in the basin centre, and the transparent eco-facies to be related to the thick Te-turbidite (clastic) and hemipelagic muds above (Fig. 4). This is consistent with previous studies that correlated similar thick acoustically-transparent layers in deep-water settings with thick turbidite deposits characterized by a thick upper clayey unit e.g., the Quaternary megaturbidites of the Mediterranean Sea (Cita et al., 1984; Cita and Rimoldi, 1997; Cita and Aloisi, 2000; Rebesco et al., 2000; Rothwell et al., 2000), the Marmara Sea (Beck et al., 2007), or the Gulf of Mexico (Tripsanas et al., 2004). The transparent echo-facies widely prevails in the centre of the basin (Figs. 2, 4). This suggests that the volume of turbidite mud is considerably more important than the volume of sand and silt in the 20°N Basin. Considering the seismic facies of M1–M20 units, their turbiditic origin (KS11) and their similarity with other deep water, Quaternary ponded deposits, the sedimentary deposits of the 20°N Basin are thus interpreted as mud-rich megaturbidites. The term "megaturbidite" is here used *sensu* the terminology of Bouma (1987), i.e. it describes exceptionally thick and/or laterally extensive layers of relatively homogeneous deposits consisting of material transported by gravity-driven density current or mass-flow.

*4.3.2. Age determination of the 20°N Basin megaturbidites*

Radiocarbon dates on cores KS11 and KS12 allows determining the age of the M1 to M5 megaturbidites (Fig. 5, Table 2), ranging from 21.2 ka BP (M1) to 35.3 ka BP (M5). Below M5, ages of M6, M7 and M8 have been obtained through correlation with the core MD04-2861 age model (Fig. 5; Caley et al., 2011). The results give an age of 85 ka BP for M8 (Table 2). Older megaturbidites could not be dated using the stratigraphic age model. However their ages can be estimated by using the evolution through time of the deformation rates on the edges of the basin. The angles of dip (in degrees) of the megaturbidite beds have been measured along the log Section 1 on the seismic profile SBP-1 (Fig. 4, Table 2). Dip values are regularly decreasing from the older megaturbidite beds (M20) to the younger (M1), suggesting constant rates of tilting on the edges of the 20°N Basin (Table 2). To test this hypothesis we measured the offset value (fault throw, in metres) of the megaturbidite beds at the location of the F1 normal fault on the seismic profile SBP-1 (Fig. 4). Results (Table 2) show that the fault throw also regularly decreases from M9 (15.1 m) to M1 (4.7 m). Linear regression between the age of megaturbidites and their offset at F1 gives an R-squared value of 0.93 (Fig. 7). These observations suggest that the subsidence (and tilting of sedimentary layers) occurred at a constant rate during the Late Quaternary. Considering a constant tilting rate, and hence dip values, increasing with time, the approximate age of pre-M8 deposits can be estimated (Fig. 7). We obtained the linear regression equation of relationship between the dipping of the megaturbidite beds and their age by using the eight dated (age model-based) deposits (M1–M8; Fig. 7). The obtained R-squared value is $>0.96$ (Fig. 7). The regression equation is then used to calculate the age of M9 to M19 deposits (Table 2). Dip values and age could not be estimated for M2 as it is too thin on the log section to be resolved with confidence at the scale of seismic data (Fig. 4). Penetration and quality of seismic signal decrease with depth hence measurement of seismic units dip angle is less accurate below M14–M15 on Section 1 (Fig. 4). Similarly, dip measurement and therefore age determination were impossible for M20 on Section 1 (Fig. 4). Thus similar measurements have been made along a second vertical log section (Section 2; Fig. 4) on the south-western edge of the profile SBP1 (Table 2). The linear regression equation of relationship between the dip of the megaturbidite beds and their age on Section 2 has been achieved by using the eight confidently dated (age model-based) deposits (M1–M8) as well as the M9–19 ages calculated from Section 1 (Table 2). The obtained R-squared value is $>0.95$ (Fig. 7). The regression equation has then been used to estimate the age of M14 to M20 deposits (Table 2), and the final age of these seismic units have been calculated as a mean of individual values obtained by the interpolation on both log sections (Table 2; Fig. 7). Using this technique, age estimation indicates that the oldest visible on the seismic data (megaturbidite event M20) is dated at 357.8 ka BP (MIS 10).

Uncertainties in age estimation increase from the youngest megaturbidites (M1–M8) to the oldest (M9–M20; Fig. 8; Table 2). M1 to M5 have been dated using radiocarbon data (Table 2). Their age uncertainty is thus given by the error in radiocarbon measurement (Table 1) and is less than 260 years. Megaturbidites 6 to 8 have been dated through core-to-core correlation with the stratigraphic reference MD04-2861 (Fig. 5). Chronostratigraphy of MD04-2861 was realized through biostratigraphy and correlation with U/Th dating in the Arabian Peninsula (Caley et al., 2011). This radioisotopic data is associated with error ranges of ca. 1 ka (Caley et al., 2011 and references therein). Age of the megaturbidites M9 to M19 were estimated at log Section 1 (Fig. 4). The uncertainty in the age determination was determined by calculating the standard deviation in the calculated ages, considering than more than 95% of the calculated error is contained within twice the standard deviation (Table 2). The mean statistical variance,

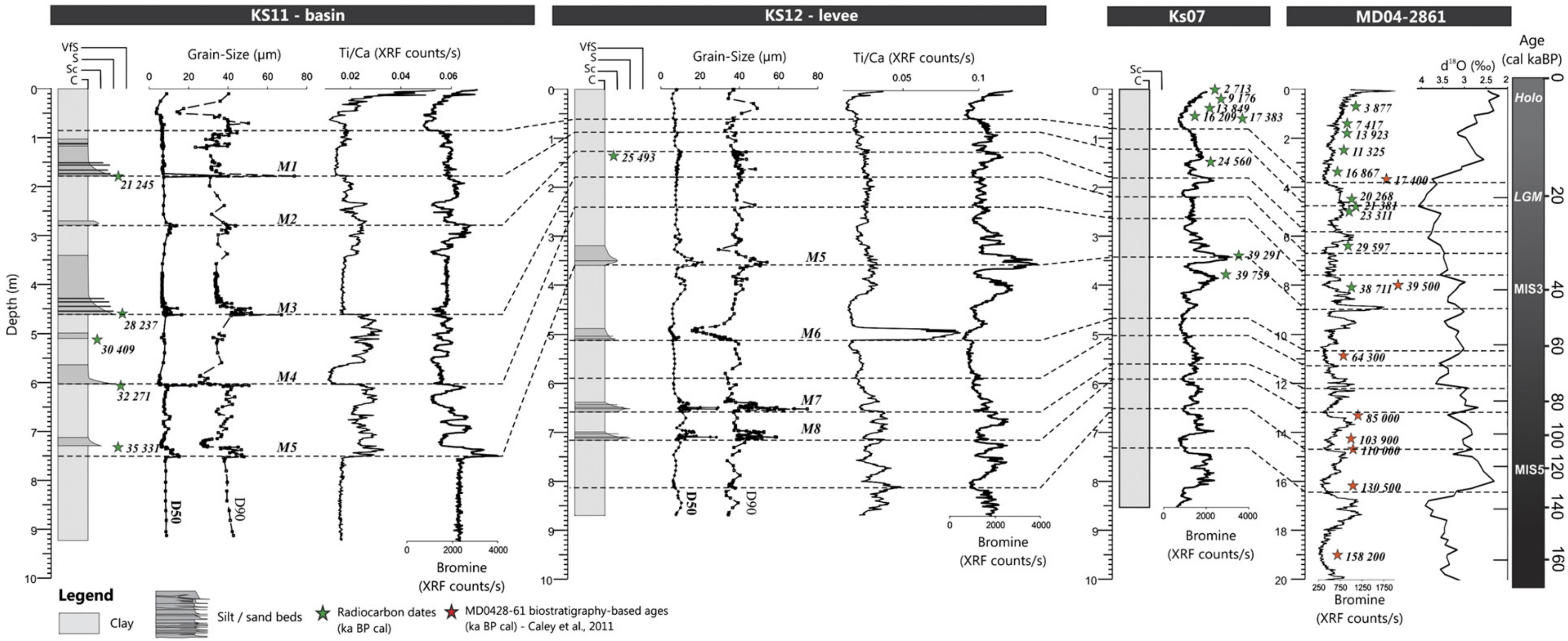


**Fig. 5.** Core correlation and stratigraphy based on grain-size measurement (D50, D90, μm), Bromine (Br) and Ti/Ca XRF measurement, radiocarbon dating and correlation with MD04-2861 regional stratigraphic reference (Caley et al., 2011).

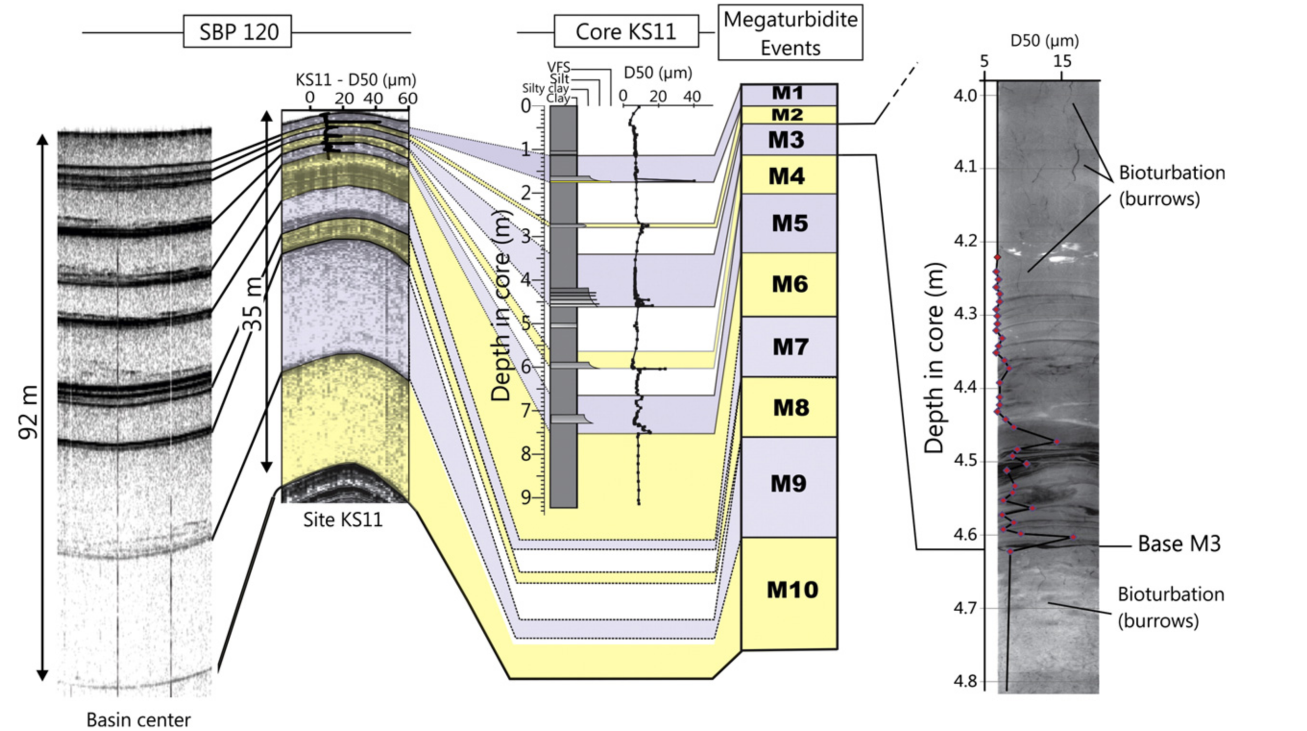


**Fig. 6.** Correlation between KS11 core data (lithology and grain-size measurement) and sub-bottom seismic reflections at site KS11 and in the centre of the 20°N Basin. Close-up on M3 megaturbidite bed showing X-ray core section and D50 (μm) grain-size measurement.

consisting of the mean of the squared differences between the estimated ages of M1–M8 at log Section 1 and their "core data" value, was first calculated. The standard deviation equals the root mean square of this value (Table 2). This provides an error range for the ages of M9–M19 of ca. 10 ka (Table 2). Uncertainty in the age of M20 was estimated by calculating the standard deviation at log Section 2 following the same method. Here the mean variance consists of the mean of the squared differences between the estimated ages of M1–M8 at log Section 2 and their "core data" value, and the estimated ages of M9–M19 at log Section 2 and their estimated age at log Section 1. Error range for M20 reaches 39 ka. However this value adds up to the error range associated with age estimation at log Section 1 (as these values were used to calculate the standard deviation at log Section 2), and the total error range for M20 is 49 ka (Table 2). These uncertainties in age determination are important when considering the timing of megaturbidite emplacement in the 20°N Basin and its relationship with sea-level or climate.

## 5. Discussion

### *5.1. Mechanisms of formation of the 20°N Basin megaturbidites: ponded lobes of the Indus Fan*

#### *5.1.1. Provenance of the turbidity currents*

The discovery of distal megaturbidite deposits at a deep-water plate boundary raises the question of the provenance of the turbidity currents at the origin of their formation. The 20°N Basin is fed by a

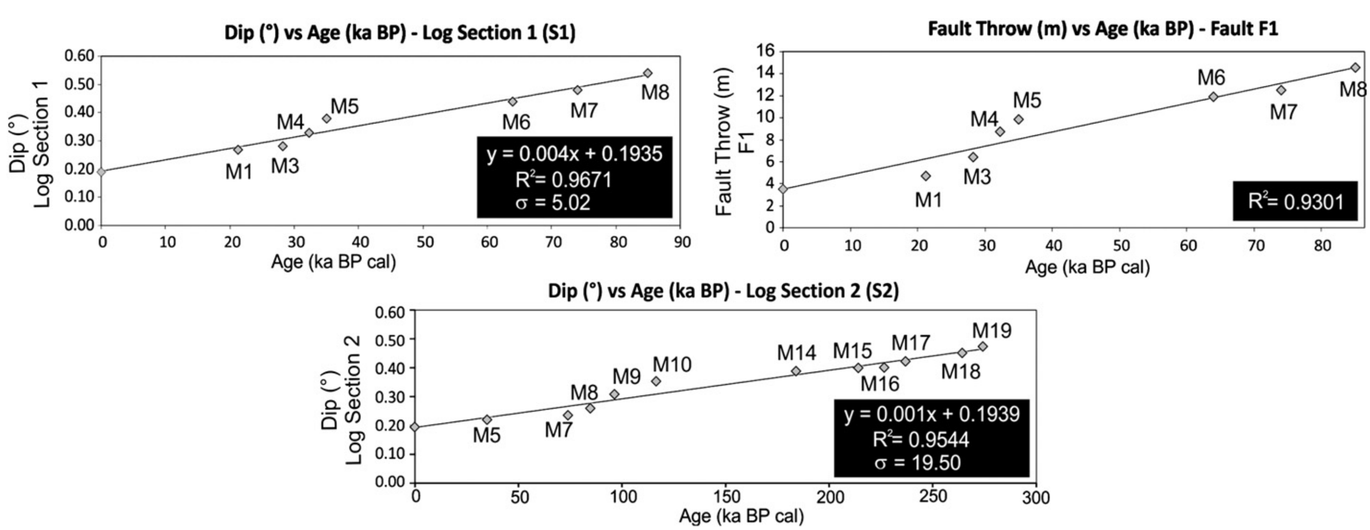


**Fig. 7.** Correlation between dip angle (°) and stratigraphic age at Log Sections 1 and 2 and between fault throw (m) and stratigraphic age at Log Section 1, showing linear regression equation and determination coefficient ($R^2$).

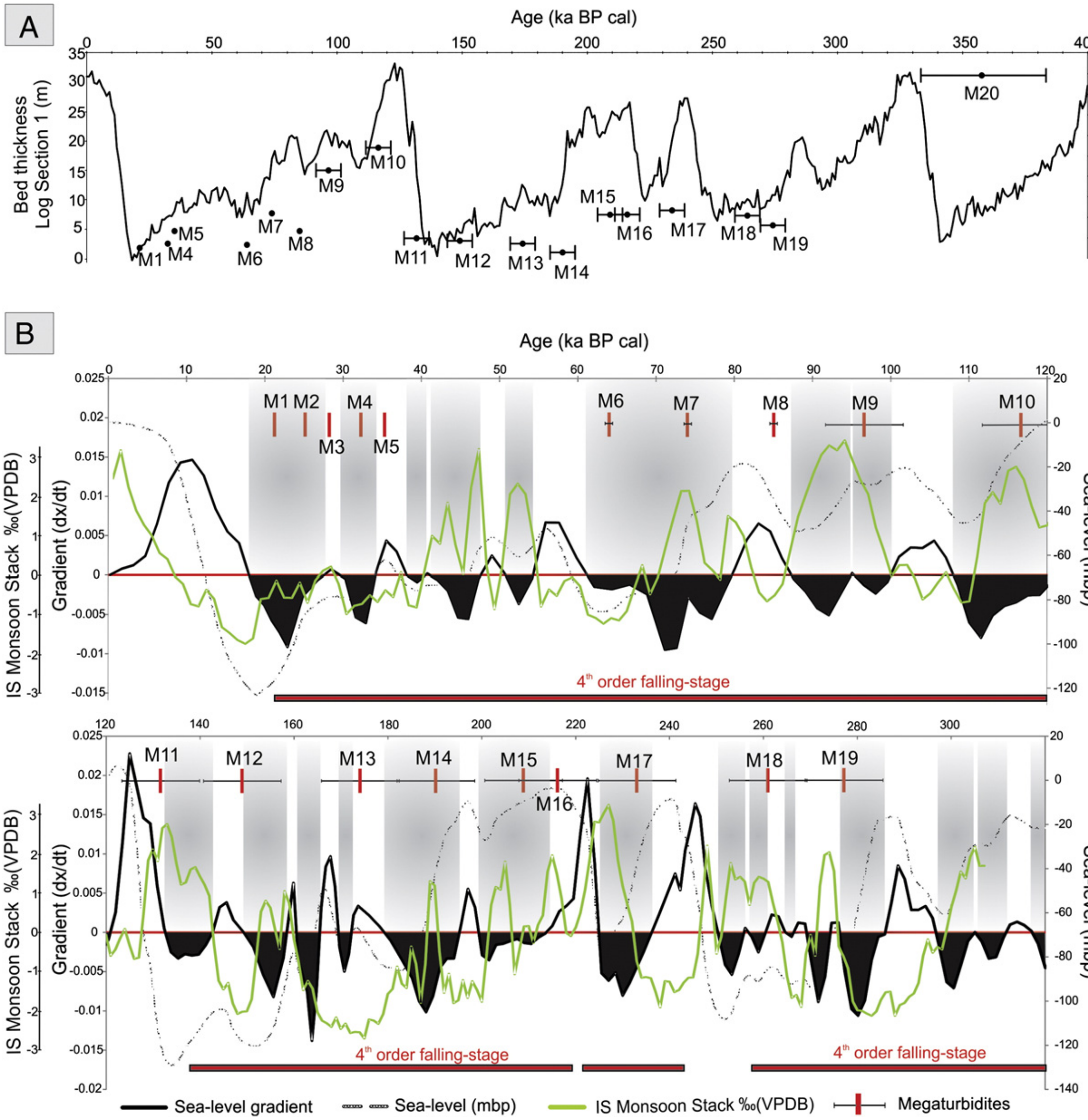


**Fig. 8.** (A) Age of 20°N Basin megaturbidites and LR04 benthic $\delta^{18}$O stack constructed by the graphic correlation of 57 globally distributed benthic $\delta^{18}$O records (Lisiecki and Raymo, 2005); (B) age of 20°N Basin megaturbidites and comparison with the global sea-level curve (in mbp – *metres below present* – from Waelbroeck et al., 2002), the sea-level gradient curve (showing periods of sea-level fall (shaded in black color), periods of sea-level rise, and still-stands), and the Indian Summer Monsoon stack from Caley et al (2011) based on core MD04-2861. Error bars on megaturbidites represent the uncertainty in age estimation (Table 2).

channel–levee system trending east to west (Fig. 3), thus indicating a possible connection with the turbidite system of the Indus Fan to the east (Fig. 1). A local origin for the 20°N Basin deposits can be ruled out as slump scars are not observed along the pull-apart basin walls and mass-transport deposits are not observed on seismic profiles (Rodriguez et al., 2011; Figs. 1, 2, 3). Bathymetry and shallow seismic data also show that there is no sediment supply from the Oman margin to the west (Rodriguez et al., 2011; Figs. 1, 3). The bathymetry data used in this study is incomplete but does not suggest a direct linkage with the main Indus canyon upslope (Fig. 1). Instead, the feeder channel of the 20°N Basin is located approximately 200 km downstream of the channel–levee systems of the Canyon system 2 mapped by Kolla and Coumes (1987) from bathymetry and sub-bottom seismic data (Fig. 1). The age of the canyon system 2 and its channel–levee systems is uncertain but the lack of channel-plug deposits on the published seismic data of Kolla and Coumes (1987) suggests that they were active recently and presumably during the Late Quaternary. This is also suggested by the more recent seismic profiles analysed by Carmichael et al. (2009) in the same area (western Indus Fan) that revealed several recent canyons and channel/levee complexes of latest Pleistocene in age (Fig. 1). Thus, it is possible that the 20°N channel was connected to distal channels from the canyon system 2 (Fig. 1) but this remains speculative due to the limitations of the data presently available and the lack of stratigraphic control in the original data of Kolla and Coumes (1987). However the data available suggest that the megaturbidites of the 20°N Basin are distal turbidite deposits of the Indus Fan.

#### 5.1.2. Ponded lobe deposits

The distal parts of deep-water turbidite systems are often associated with the formation of channel-mouth lobe complexes. The latter form depositional areas where sands are generally concentrated as the gravity currents have been progressively depleted in fine-grained sediments through overbank processes along the channel–levee systems. Along mud-rich, passive margin turbidite systems such as the Indus Fan, channel-mouth lobes develop across unconfined basin plains and generally extend over very large distances, exceeding 100 km on the Amazon, Nile, Zaire or Mississippi fans (Twichell et al., 1991; Savoye et al., 2000; Jegou et al., 2008; Migeon et al., 2010). These lobes typically form highly ramified, channelized and elongated depositional environments. In the Indus Fan, deep sea lobes from the last active channel/levee complexes (CLC A and B) also developed over very large distances across the very low gradient, eastern basin plain (Kenyon et al., 1995). Conversely the last active channel–levee system in the study area abruptly terminates its course in a very confined trough, less than 13 km-wide and up to 320 m-deep at this location (Fig. 1). Individual lobe deposits in mud-rich fans are dispersed over very large distances (>100 km) and form relatively thin (typically cm to dm-thick) deposits (Twichell et al., 1991; Bonnel, 2005; Migeon et al., 2010). However the range of thicknesses and volumes of individual lobe deposits in other mud-rich fans approaches the values obtained in the 20°N Basin. A 20 cm, 50 cm, or 1 m thick turbidite (e.g., range of lobe thickness deposits in mud-rich deep-sea lobes; Twichell et al., 1991; Bonnel, 2005; Migeon et al., 2010) deposited within a lobe area of 4800 $km^2$ (the size of the Nile deep-sea lobes off the Rosetta channel–levee complex; Migeon et al., 2010) represent a volume of 0.96, 2.4, and 4.8 $km^3$, respectively. This is of similar if not higher order of magnitude than the values calculated for M1–M8 megaturbidites in the 20°N Basin (0.4 to 2.79 $km^3$; Table 2), which is only 260 $km^2$ in area (Fig. 1). Thus the great thickness of each turbidite event in the 20°N Basin is more likely related to the confinement of the depositional area rather than to an exceptional volume of sediment transported by gravity currents. Therefore, the Indus megaturbidites differ from the previously described megaturbidites of the Quaternary that are usually thinner (7 m-thick deposit on average) but laterally extensive (51,000 $km^2$ on average) and are rather similar to ancient megaturbidites, generally thicker (average 40 m) but deposited in confined basins (435 $km^2$ on average; Reeder et al., 2000; Mulder et al., 2009). Considering the volume of individual turbidite deposits in the 20°N Basin, it is unlikely that turbidity currents at their origin were formed through local mass-reworking of levee deposits from the upper Indus Fan, although it is possible that downslope erosion along the turbidity current pathway may have contributed to the final turbiditic volumes observed in the 20°N Basin. The thick, acoustically-transparent seismic facies of the 20°N Basin megaturbidites is a characteristic often observed in ponded turbidites deposits (e.g., Cita and Aloisi, 2000; Tripsanas et al., 2004; Beck et al., 2007). Thick acoustically-transparent layers correspond to ungraded, often structureless clastic muds representing fallout from a suspension cloud produced by axial ponding of the muddy tail of turbidity currents (Pickering and Hiscott, 1985; Haughton, 1994; Mulder et al., 2009). Therefore, the capture of a distal Indus turbidite channel by the 20°N pull-apart basin resulted in the formation of the very thick (individually up to 20 m), mud-rich megaturbidite beds through flow ponding in a confined trough. These form unusual deposits equivalent to distal "lobe" deposits trapped at a transform (strike-slip) plate boundary.

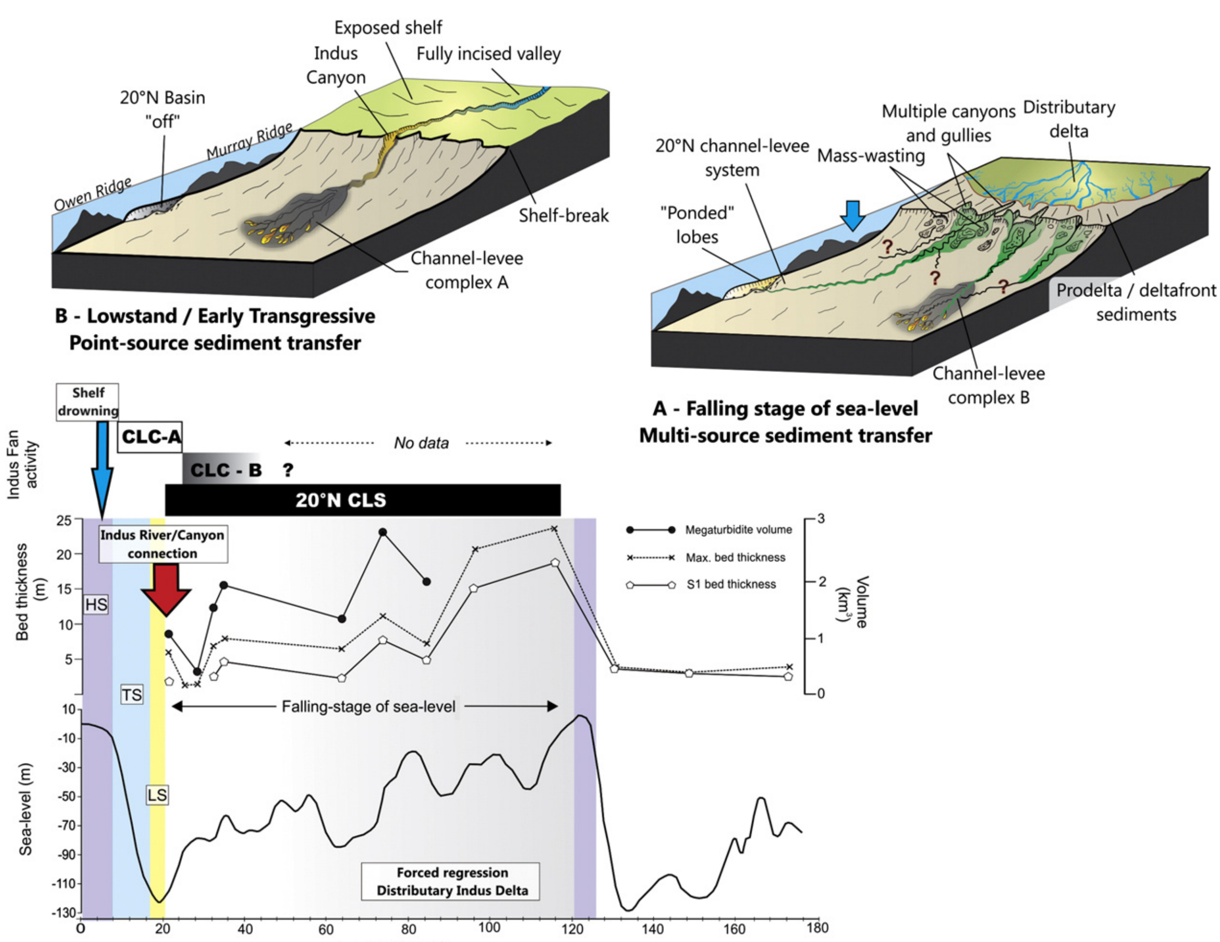


**Fig. 9.** Late Quaternary (last 122 ka BP) evolution of the Indus Delta and turbidite system: comparison between the measured thicknesses of 20°N megaturbidite deposits at Log Section 1 (S1, m) and in the basin centre (Max. bed thickness, m), their estimated volume ($km^3$) and the relative sea-level curve (m below its present-day position) from Waelbroeck et al. (2002). Periods of activity of the channel–levee complexes A and B (Kenyon et al., 1995; Prins and Postma, 2000; Prins et al., 2000) and 20°N Basin (this study) are indicated. LS = sea-level lowstand; TS = transgression; HS = sea-level highstand.

### 5.2. Late Quaternary evolution of the Indus Fan and stratigraphic significance of the 20°N Basin megaturbidites

#### 5.2.1. Link between the 20°N megaturbidites, sea-level and climate

The comparison of the age and thickness of the best dated sequence of megaturbidites of the 20°N Basin (M1–M10) with the oxygen isotope and sea-level record of the Late Quaternary primarily shows two main trends (Figs. 8 & 9). Firstly, the deposition of the megaturbidites occurred within the context of a 4th-order (ca. 100 ka-duration) falling-stage of sea-level period (Figs. 8 & 9). In addition, the maximum bed thickness of the megaturbidites (measured in the basin centre), their bed thickness measured at log Section 1, and their estimated volume all globally decrease with their age (Figs. 8 & 9). These observations suggest that the volume of sediments brought by individual turbidity current to the 20°N Basin decreased with time as the sea-level felt (i.e., in conditions of forced regression). These trends are less pronounced for older megaturbidites (M11–M20; Fig. 8). Measurements at log Section 1 show that within megaturbidites deposited during the previous sea-level fall period (ca. 216–128 ka BP), M15 and M16 are thicker (7.5 m) than M14–M11 (0.9–3.5 m). Megaturbidites M17–M20 were formed in different 4th-order falling sea-level periods, where the low number of megaturbidites recorded precludes drawing significant conclusions (Fig. 8). Whether the 20°N Basin megaturbidites were deposited in conditions of high-frequency sea-level fall, rise or stillstand is more difficult to apprehend considering the limitations of the dataset. In particular, the error ranges associated with the age calculations for megaturbidites M9 to M19 (10 ka) and M20 (49 ka) need to be taken in account (Fig. 8). A gradient curve was calculated from the sea-level curve of Waelbroeck et al. (2002) in order to identify periods and rates of sea-level changes at high-frequency (Fig. 8). The results show that the age of 5 out of 8 (62.5%) of the best dated sequences (M1–M8) corresponds to a period of sea-level fall (Fig. 8). Similarly, eight out of eleven (72%) megaturbidites with higher uncertainty in age estimation (M9–19) correspond to periods of sea-level fall (with more than 50% of their age range coinciding with falling-stage periods; Fig. 8). In conclusion, the comparison between megaturbidite emplacement in the 20°N Basin and sea-level changes suggest that megaturbidites were formed during 4th-order sea-level fall periods, but their link with high-frequency sea-level changes is difficult to establish, maybe due to the low number of events and the errors in age estimation (Figs. 8 & 9).

The possible linkage between the timing of megaturbidite emplacement and climate-induced periods of increased sediment discharge in the Indus catchment is another interesting parameter to investigate. Indeed, monsoon-induced humid periods directly influenced the Late Quaternary evolution of basinward sediment transfer along the nearby Makran margin, resulting in more frequent, finer-grained turbidite system growth (Bourget et al., 2010). Similar monsoon-induced control on turbidite system growth was observed in the Nile turbidite system (Ducassou et al., 2009). However, the Indus River catchment includes the western part of the Himalayan orogen where glaciers develop (Benn and Owen, 1998; Owen et al., 2008). Continental record shows that the timing of glaciation within the Indus River catchment during the Late Quaternary was not synchronous with the global ice-volume maximum (Benn and Owen, 1998). Instead, regional glacier expansion coincided with the Northern Hemisphere insolation maxima and periods of enhanced summer monsoon (Benn and Owen, 1998; Owen et al., 2008). The increase in precipitation rates in the very high altitude Indus River catchment was associated with snowing and glacial advance (Owen et al., 2008). Therefore, maximum river discharge at the Indus River mouth and periods of increased turbidite system growth would coincide with melt-water pulses in deglacial periods, as is commonly observed in glacial-influenced turbidite systems of the Northern Hemisphere (e.g., Zaragosi et al., 2006). However, the comparison of the megaturbidite stratigraphy with the Indian Summer Monsoon stack of Caley et al. (2011) does not show any significant relationship between summer monsoon intensity and the 20°N Basin megaturbidites (Fig. 8). The megaturbidites do not systematically form following a peak in summer monsoon intensity (i.e., a likely melt-water pulse event) and no clear trend can be observed (Fig. 8). However this apparent lack of correlation could be the result of the error ranges in age estimation, as well as the very distal location of the 20°N Basin with regards to the Indus Delta (Fig. 1).

#### 5.2.2. A progressive confinement of sediment supply to the basin during the last sea-level cycle?

The 20°N Basin megaturbidites have been deposited during 4th-order periods of falling sea-level (Figs. 8 & 9). The best dated sequence, which corresponds to the last ten events (M1–M10), shows a decrease in megaturbidite thickness and volumes during the last sea-level fall period of the Quaternary. This stratigraphic evolution forms two apparent paradoxes:(i) the presence of a thinning-upward deep-water sequence within a period of forced-regression and increase in source-to-sink sediment transfer (Posamentier and Kolla, 2003; Catuneanu et al., 2009), and (ii) the cessation of turbidite activity in the 20°N Basin at the onset of the LGM, whilst the Indus River directly discharged sediments into the Indus Canyon and led to maximum fan aggradation into the basin (Kenyon et al., 1995; Prins and Postma, 2000; Prins et al., 2000). To understand this phenomenon, the linkage between the 20°N Basin and the upstream part of the Indus Fan need to be investigated, and the megaturbidites need to be replaced in the context of global evolution of the Indus sedimentary system during the Late Quaternary (Fig. 9).

Recent evolution of the Indus Delta has been marked by basinward progradation with 98% of the Indus River pre-damming sediment load being deposited in delta front (86%) and prodelta (13%) clinoforms (Giosan et al., 2006). Thus Holocene sedimentation in the Indus Delta corresponds to typical conditions of stillstand normal regression (Posamentier et al., 1989; Posamentier and Kolla, 2003; Catuneanu et al., 2009). Sediments are temporarily stored along the continental shelf during this highstand period and deep-water sediment deposition is therefore very limited, and restricted to occasional flushing of delta-front and pro-delta sediments in the Indus Canyon (von Rad and Tahir, 1997; Prins et al., 2000). Indus Delta-basin configuration during the MIS 5 sea-level highstand was likely similar to the present day conditions. The following onset of sea-level drop at ~122 ka BP was associated with forced regression of the delta (von Rad and Tahir, 1997), where either multiple river distributaries and/or tidal reworking could have created multiple points of sediment entry in the outer shelf (Fig. 9). Indeed, von Rad and Tahir (1997) mapped numerous buried or semi-buried channels and gullies west and east of the main Indus Canyon. Their results showed that they were formed during the last ~122 ka BP, and prior to the Last Glacial Maximum lowstand, in conditions of high rates of delta front/prodelta progradation and high sediment supply. This period was also associated with widespread mass-wasting in the upper-slope area (von Rad and Tahir, 1997). High sediment supply rates were likely enhanced by both rapid progradation of the Indus Delta toward the shelf-break and remobilization of the large volumes of delta-front and pro-delta fine-grained sediments accumulated on the continental shelf during the preceding highstand. It is also possible that other canyon systems were active during this period (Fig. 9), including the canyon system 2 (Fig. 1) of Kolla and Coumes (1987), although this remains speculative due to the lack of age control. Basinward, both channel–levee complex B, to the east (Kenyon et al., 1995; Prins et al., 2000) and the 20°N channel–levee system, to the west (this study) were synchronously active (Fig. 9). Thus turbidity currents originated from the Indus Delta were transported through at least two different channel–levee systems to the south-east (CLC B) and west (20°N channel) prior to the Last Glacial Maximum, in addition to the multiple shelf-edge canyon and gullies mapped by von Rad and Tahir (1997). The combination of the results obtained in the present study with previously published data suggests that during the last falling stage of sea-level period, the Indus Fan consisted of a delta-fed turbidite system with several active canyons-channels system (Fig. 9).

According to Prins et al. (2000), avulsion from CLC B to CLC A occurred at around 28 ka BP, i.e. during period of rapid sea-level fall of about 60 m (Lea et al., 2002; Waelbroeck et al., 2002; Clark et al., 2009) that likely promoted shelf incision and erosion. This age is also only slightly younger than the age of the last turbiditic deposit the 20°N Basin (21.2 ka BP; Fig. 9). During the following sea-level lowstand and early transgression periods, the channel–levee systems of CLC A are the only known active turbidity current pathways (Prins et al., 2000). This suggests that the Indus Fan ultimately evolved from a multiple-source, delta-fed turbidite system to a point source, "river-canyon" turbidite system following the abrupt drop in sea-level at MIS 3/2 transition (Fig. 9). We infer that the last thinning-upward sequence in the 20°N Basin reflects the local, progressive diminution of sediment supply at the source of the 20°N Basin channel, as the Indus Delta evolved from a distributary delta (multiple points of sediment entry) to a single-channelled, incised valley system (one unique point of sediment entry in the Indus Canyon). The observation of two vertically-stacked thinning-upward megaturbidite sequences on seismic profiles (M1–M10, M11–M20; Figs. 2 & 4) suggests that this sea-level controlled depositional evolution could have repeated during the Quaternary. However age estimation for megaturbidite M20 falls out of the 330–135 ka BP falling-stage of sea-level sequence (Fig. 8). This result could highlight a discontinuous sediment supply to the 20°N Basin between 357 and 277 ka BP (Fig. 8), but could also be related to an overestimated M20 age caused by non-steady-state local deformation rates.

The megaturbidite depositional history of the 20°N Basin generally reflects a diminution of local sediment supply through times, during periods of global increase in sediment supply in the basin (Fig. 8). This highlights the importance of delta evolution during forced regressions (river entrenchment) for the spatial and temporal distribution of deep-water sediments.

## 6. Conclusion

The formation of a pull-apart basin at the Arabian-Indian transform plate boundary led to the capture of a Late Quaternary channel–levee system from the Indus Fan. Architecture of the 20°N Basin consists of a vertical stack of up to 23 m thick megaturbidites laterally confined in a 260 km$^2$ basin. Each of these beds corresponds to the deposition from a single gravity current. Unlike most of the previously described megaturbidites of the Quaternary, 20°N Basin deposits do not result from exceptionally large volumes of sediment reworked through mass-wasting processes. Conversely, they are related to the ponding of "classical" turbidity currents transported along a sinuous channel–levee system that abruptly terminates in a distal, confined pull-apart basin. Therefore they form unusual, "ponded" lobe deposits from the Indus Fan. The ten most recent megaturbidites have been deposited during the last falling stage of sea-level cycle. Both thickness and volume of each individual megaturbidite is decreasing through the last 122 ka BP. Local turbidite deposition ceases after 21 ka, i.e. during the sea-level lowstand period, when the Indus River was directly connected to the Indus Canyon enhancing maximum sediment transfer to the deep basin. This apparent paradox is analyzed in terms of sea-level control on source-to-sink sediment dispersal modes in the Indus sedimentary system. At least two channel–levee systems were active during the last falling stage of sea-level period, and were fed by a prograding delta (forced regression) with multiple points of sediment entry distributed along the outer shelf and shelf-break. Turbidite transfer locally decreased within these systems as the Indus River became increasingly entrenched in an incised valley and progressively focused its sediment discharge into the Indus Canyon. This led to the disconnection of the older channel–levee systems and development of a point-source turbidite system that remained active throughout the lowstand and early transgressive stages. This work shed new light on the recent evolution of the Indus sedimentary system and illustrates the importance of sea-level control on the sedimentary transfer mechanisms during forced regressive periods.

## Acknowledgment

We are indebted to all the crew from the "Owen" and "FanIndien" surveys 2009 (*BHO Beautemps-Beaupré*) for their assistance in data acquisition. We thank Peter Talling, an anonymous reviewer and the editor D. J. W Piper for their insightful reviews that greatly improved the paper.

## References

Beck, C., Mercier de Lepinay, B., Schneider, J.-L., Cremer, M., Cagatay, N., Wendenbaum, E., et al., 2007. Late Quaternary co-seismic sedimentation in the Sea of Marmara's deep basins. Sedimentary Geology 199, 65–89.
Benn, D.I., Owen, L.A., 1998. The role of the Indian summer monsoon and the mid-latitude westerlies in Himalayan glaciation: review and speculative discussion. Journal of the Geological Society of London 155, 353–363.
Bonnel, C., 2005. Mise en place des lobes distaux dans les systèmes turbiditiques actuels: Analyse comparée des systèmes du Zaïre, Var et Rhône. Unpublished Ph.D Thesis, Université Bordeaux 1, p. 314.
Bouma, A.H., 1962. Sedimentology of Some Flysch Deposits: A Graphic Approach to Facies Interpretation. Elsevier, Amsterdam.
Bouma, A.H., 1985. Introduction of submarine fans and related Turbidite facies. In: Bouma, A.H., Barnes, N.E., Normark, W.R. (Eds.), Submarine Fans and Related Turbidite Sequences. SpringerVerlag, NewYork, pp. 3–5.
Bouma, A.H., 1987. Megaturbidite: an acceptable term? Geo-Marine Letters 7, 63–67.
Bouma, A.H., Stelting, C.E., Coleman, J.M., 1985. Mississippi fan: Gulf of Mexico. In: Bouma, A.H., Barnes, N.E., Normark, W.R. (Eds.), Submarine Fans and Related Turbidite Sequences. Springer-Verlag, NewYork, pp. 143–150.
Bourget, J., Zaragosi, S., Garlan, T., Gabelotaud, I., Guyomard, P., Dennielou, B., et al., 2008. Discovery of a giant deep-sea valley in the Indian Ocean, off eastern Africa: the Tanzania channel. Marine Geology 255, 179–185.
Bourget, J., Zaragosi, S., Ellouz-Zimmermann, S., Ducassou, E., Prins, M.A., Garlan, T., et al., 2010. Highstand vs. lowstand turbidite system growth in the Makran active margin: Imprints of high-frequency external controls on sediment delivery mechanisms to deep water systems. Marine Geology 274, 187–208.
Bourget, J., Mouchot, N., Zaragosi, S., Ellouz-Zimmermann, N., Garlan, T., Lanfumey, V., VanToer, A., Schneider, J.-L., 2011. Turbidite system architecture and sedimentary processes along topographically complex slopes: the Makran convergent margin. Sedimentology 58 (2), 376–406.
Boyd, R., Ruming, K., Goodwin, I., Sandstrom, M., Schröder-Adams, C., 2008. Highstand transport of coastal sand to the deep ocean: a case study from Fraser Island, southeast Australia. Geology 36, 15–18.
Caley, T., Malaizé, B., Zaragosi, S., Rossignol, L., Bourget, J., Eynaud, F., et al., 2011. New Arabian Sea records help decipher orbital timing of Indo-Asian monsoon. Earth and Planetary Science Letters 308, 433–444.
Carmichael, S.M., Akhter, S., Bennett, J.K., Fatimi, M.A., Hosein, K., Jones, R.W., et al., 2009. Geology and hydrocarbon potential of the offshore Indus Basin, Pakistan. Petroleum Geoscience 15, 107–116.
Catuneanu, O., Abreu, V., Bhattacharya, J.P., Blum, M.D., Dalrymple, R.W., Eriksson, P.G., et al., 2009. Towards the standardization of sequence stratigraphy. Earth-Science Reviews 92, 1–33.
Cita, M.B., Aloisi, G., 2000. Deep-sea tsunami deposits triggered by the explosion of Santorini (3500 y BP), eastern Mediterranean. Sedimentary Geology 135, 181–203.
Cita, M.B., Rimoldi, B., 1997. Geological and geophysical evidence for a holocene tsunami deposit in the astern Mediterranean deep-sea record. Journal of Geodynamics 24, 293–304.
Cita, M.B., Beghi, C., Camerlenghi, A., Kastens, K.A., McCoy, F.W., Nosetto, A., et al., 1984. Turbidites and megaturbidites from the Herodotus abyssal plain (eastern Mediterranean) unrelated to seismic events. Marine Geology 55, 79–101.
Clark, P.U., Dyke, A.S., Shakun, J.D., Carlson, A.E., Clark, J., Wohlfarth, B., et al., 2009. The Last Glacial Maximum. Science 325, 710–714.
Clift, P.D., Shimizu, N., Layne, G.D., Blusztajn, J.S., Gaedicke, C., Schluter, H.-U., et al., 2001. Development of the Indus Fan and its significance for the erosional history of the Western Himalaya and Karakoram. Geological Society of America Bulletin 113, 1039–1051.
Clift, P., Gaedicke, C., Edwards, R., Lee, J.I., Hildebrand, P., Amjad, S., et al., 2002. The stratigraphic evolution of the Indus fan and the history of sedimentation in the Arabian Sea. Marine Geophysical Researches 223–245.
Coumes, F., Kolla, V., 1984. Indus Fan: seismic structure, channel migration and sediment thickness in the upper fan. In: Haq, B.U., Milliman, J.D. (Eds.), Van Nostrand Reinhold Comp., New York, pp. 101–110.
Droz, L., Mougenot, D., 1987. Mozambique upper fan: origin of depositional units. AAPG Bulletin 71, 1355–1365.
Ducassou, E., Migeon, S., Mulder, T., Murat, A., Capotondi, L., Bernasconi, S.M., et al., 2009. Evolution of the Nile deep-sea turbidite system during the Late Quaternary: influence of climate change on fan sedimentation. Sedimentology 56, 2061–2090.

Fournier, M., Chamot-Rooke, N., Petit, C., Fabbri, O., Huchon, P., Maillot, B., et al., 2008. In situ evidence for dextral active motion at the Arabia–India plate boundary. Nature Geoscience 1, 54–58.

Fournier, M., Chamot-Rooke, N., Rodriguez, M., Huchon, P., Petit, C., Beslier, M.O., et al., 2011. Owen fracture zone: the Arabia–India plate boundary unveiled. Earth and Planetary Science Letters 302, 247–252.

Giosan, L., Constantinescu, S., Clift, P.D., Tabrez, A.R., Danish, M., Inam, A., 2006. Recent morphodynamics of the Indus delta shore and shelf. Continental Shelf Research 26, 1668–1684.

Goldfinger, C., Nelson, C.H., Johnson, J.E., Party, T.S.S., 2003. Holocene earthquake records from the Cascadia subduction zone and northern San Andreas fault based on precise dating of offshore turbidites. Annual Review of Earth and Planetary Sciences 31, 55–77.

Haughton, P., 1994. Deposits of deflected and ponded turbidity currents, Sorbas basin, southeast Spain. Journal of Sedimentary Research A64, 233–246.

Jegou, I., Savoye, B., Pirmez, C., Droz, L., 2008. Channel–mouth lobe complex of the recent Amazon Fan: the missing piece. Marine Geology 252, 62–77.

Karim, A., Veizer, J., 2002. Water balance of the Indus River Basin and moisture source in the Karakoram and western Himalayas: implications from hydrogen and oxygen isotopes in river water. Journal of Geophysical Research 107, 4362.

Kenyon, N.H., Amir, A., Cramp, A., 1995. Geometry of the younger sediment bodies of the Indus Fan. In: Pickering, K.T., Hiscott, R.N., Kenyon, N.H., Ricci Lucchi, F., Smith, R.D.A. (Eds.), Atlas of Deep Water Environments: Architectural Style in Turbidite Systems. Chapman & Hall, London, pp. 89–90.

Khripounoff, A., Vangriesheim, A., Babonneau, N., Crassous, P., Dennielou, B., Savoye, B., 2003. Direct observation of intense turbidity current activity in the Zaire submarine valley at 4000 m water depth. Marine Geology 194, 151–158.

Kolla, V., Coumes, F., 1987. Morphology, internal structure, seismic stratigraphy, and sedimentation of Indus Fan. AAPG Bulletin 650–677.

Kolla, V., Kostecki, J.A., Henderson, L., Hess, L., 1980. Morphology and Quaternary sedimentation of the Mozambique Fan and environs, southwestern Indian Ocean. Sedimentology 27, 357–378.

Lea, D.W., Martin, P.A., Pak, D.K., Spero, H.J., 2002. Reconstructing a 350 ky history of sea level using planktonic Mg/Ca and oxygen isotope records from a Cocos Ridge core. Quaternary Science Reviews 21, 283–293.

Lisiecki, L.E., Raymo, M.E., 2005. A Pliocene–Pleistocene stack of 57 globally distributed benthic $^{18}O$ records. Paleoceanography 20, 1–17.

Mas, V., Mulder, T., Dennielou, B., Schmidt, S., Khripounoff, A., Savoye, B., 2010. Multiscale spatio-temporal variability of sedimentary deposits in the Var turbidite system (North-Western Mediterranean Sea). Marine Geology 275, 37–52.

McHargue, T.R., Webb, J.E., 1986. Internal geometry, seismic facies, and petroleum potential of canyons and inner fan channels of the Indus submarine fan. AAPG Bulletin 161–180.

Migeon, S., Ducassou, E., Le Gonidec, Y., Rouillard, P., Mascle, J., Revel-Rolland, M., 2010. Lobe construction and sand/mud segregation by turbidity currents and debris flows on the western Nile deep-sea fan (Eastern Mediterranean). Sedimentary Geology 229, 124–143.

Milliman, J.D., Quraishee, G.S., Beg, M.A.A., 1984. Sediment discharge from the Indus River to the ocean: past, present and future. In: Haq, B.U., Milliman, J.D. (Eds.), Marine Geology and Oceanography of Arabian Sea and Coastal Pakistan. Van Nostrand Reinhold, New York, pp. 65–70.

Mulder, T., Zaragosi, S., Razin, P., Grelaud, C., Lanfumey, V., Bavoil, F., 2009. A new conceptual model for the deposition process of homogenite: application to a cretaceous megaturbidite of the western Pyrenees (Basque region, SW France). Sedimentary Geology 222, 263–273.

Normark, W.R., 1978. Fan valleys, channels, and depositional lobes on modern submarine fans: characters for recognition of sandy turbidites environments. AAPG Bulletin 62, 912–931.

Owen, L.A., Caffee, M.W., Finkel, R.C., Seong, Y.B., 2008. Quaternary glaciation of the Himalayan–Tibetan orogen. Journal of Quaternary Science 23, 513–531.

Peakall, J., McCaffrey, B., Kneller, B., 2000. A process model for the evolution, morphology, and architecture of sinuous submarine channels. Journal of Sedimentary Research 70, 434–448.

Pickering, K.T., Hiscott, R.N., 1985. Contained (reflected) turbidity currents from the Middle Ordovician Cloridorme Formation, Quebec, Canada: an alternative to the antidune hypothesis. Sedimentology 32, 373–394.

Piper, D.J.W., Normark, W.R., 2001. Sandy fans–from Amazon to Hueneme and beyond. AAPG Bulletin 85, 1407–1438.

Pirmez, C., Flood, R.D., 1995. Morphology and structure of Amazon Channel. In: Flood, R.D., Piper, D.J.W., Klaus, A., et al. (Eds.), Proceedings of the Ocean Drilling Program, Initial Reports. Ocean Drilling Program, College Station, TX, pp. 23–45.

Posamentier, H.W., Kolla, V., 2003. Seismic geomorphology and stratigraphy of depositional elements in deep-water settings. Journal of Sedimentary Research 73, 367–388.

Posamentier, H.W., Jervey, M.T., Vail, P.R., 1989. Eustatic controls on clastic deposition I — conceptual framework. In: Wilgus, C.K., et al. (Ed.), Sea-Level Changes: An Integrated Approach. SEPM Special Publication, Tulsa, pp. 110–124.

Posamentier, H.W., Erskine, R.D., Mitchum, R.M.J., 1991. Models for submarine-fan deposition within a sequence-stratigraphic framework. In: Weimer, P., Link, M.H. (Eds.), Seismic Facies and Sedimentary Processes of Submarine Fans and Turbidite Systems. Spring-Verlag, New York, pp. 127–136.

Prins, M.A., Postma, G., 2000. Effects of climate, sea level, and tectonics unraveled for last deglaciation turbidite records of the Arabian Sea. Geology 375–378.

Prins, M.A., Postma, G., Cleveringa, J., Cramp, A., Kenyon, N.H., 2000. Controls on terrigenous sediment supply to the Arabian Sea during the late Quaternary: the Indus Fan. Marine Geology 169, 327–349.

Reading, H.G., Richards, M., 1994. Turbidites systems in deep-water basin margins classified by grain size and feeder system. AAPG Bulletin 792–822.

Rebesco, M., Vedova, B.D., Cernobori, L., Aloisi, G., 2000. Acoustic facies of Holocene megaturbidites in the Eastern Mediterranean. Sedimentary Geology 135, 65–74.

Reeder, M.S., Rothwell, R.G., Stow, D.A.V., 2000. Influence of sea level and basin physiography on emplacement of the late Pleistocene Herodotus Basin Megaturbidite, SE Mediterranean Sea. Marine and Petroleum Geology 17, 199–218.

Reimer, P.J., Baillie, M.G.L., Bard, E., Bayliss, A., Beck, J.W., Blackwell, P.G., et al., 2009. IntCal09 and Marine09 radiocarbon age calibration curves, 0–50,000 years cal BP. Radiocarbon 51, 1111–1154.

Richter, T.O., Van der Gaast, S.J., Koster, B., Vaars, A.J., Gieles, R., De Stigter, H.C., et al., 2006. The Avaatech XRF Core Scanner: technical description and applications to NE Atlantic sediments. In: Rothwell, R.G. (Ed.), New Techniques in Sediment Core Analysis. Special Publications. Geological Society, London, pp. 39–50.

Rodriguez, M., Fournier, M., Chamot-Rooke, N., Huchon, P., Bourget, J., Sorbier, M., et al., 2011. Neotectonics of the Owen Fracture Zone (NW Indian Ocean): structural evolution of an oceanic strike-slip plate boundary. Geochemistry, Geophysics, Geosystems 12, 1–24.

Rodriguez, M., Fournier, M., Chamot-Rooke, N., Huchon, P., Zaragosi, S., Rabaute, A., 2012. Mass wasting processes along the Owen Ridge (Northwest Indian Ocean). Marine Geology 326–328, 80–100.

Rothwell, R.G., Reeder, M.S., Anastasakis, G., Stow, D.A.V., Thomson, J., Kahler, G., 2000. Low sea-level stand emplacement of megaturbidites in the western and eastern Mediterranean Sea. Sedimentary Geology 135, 75–88.

Savoye, B., Cochonat, P., Apprioual, R., Bain, O., Baltzer, A., Bellec, V., et al., 2000. Structure et evolution recente de l'eventail turbiditique du Zaire: premiers resultats scientifiques des missions d'exploration Zaiango1 & 2 (marge Congo-Angola) Structure and recent evolution of the Zaire deep-sea fan: preliminary results of the ZaiAngo 1 & 2 cruises (Angola-Congo margin). Comptes Rendus de l'Academie des Sciences – Series IIA – Earth and Planetary Science 331, 211–220.

Stuiver, M., Reimer, P.J., Bard, E., Beck, J.W., Burr, G.S., Hughen, K.A., et al., 1998. INTCAL98 radiocarbon age calibration, 24,000–0 cal BP. Radiocarbon 40, 1041–1083.

Tripsanas, E.K., Bryant, W.R., Phaneuf, B.A., 2004. Depositional processes of uniform mud deposits (unifites), Hedberg Basin, northwest Gulf of Mexico: New perspectives. AAPG Bulletin 88, 825–840.

Twichell, D.C., Kenyon, N., H., Parson, L.M., McGregor, B.A., 1991. Depositional patterns of the Mississippi Fan surface: evidence from GLORIA II and high-resolution seismic profiles. In: Weimer, P., Link, M.H. (Eds.), Seismic Facies and Sedimentary Processes of Submarine Fans. Springer-Verlag, New York, pp. 349–363.

Vail, P.R., Mitchum, R.M., 1977. Seismic stratigraphy and global changes of sea-level, Part 1: overview. In: Payton, C.E. (Ed.), Seismic Stratigraphy — Applications to hydrocarbon exploration. AAPG Memoir, Tulsa.

von Rad, U., Tahir, M., 1997. Late Quaternary sedimentation on the outer Indus shelf and slope (Pakistan): evidence from high-resolution seismic data and coring. Marine Geology 138, 193–236.

Waelbroeck, C., Labeyrie, L., Michel, E., Duplessy, J.C., McManus, J.F., Lambeck, K., et al., 2002. Sea-level and deep water temperature changes derived from benthic foraminifera isotopic records. Quaternary Science Reviews 21, 295–305.

Wells, J.T., Coleman, J.M., 1984. Deltaic morphology and sedimentology, with special reference to the Indus River delta. In: Haq, B.U., Milliman, J.D. (Eds.), Marine Geology and Oceanography of Arabian Sea and Coastal Pakistan. Van Nostrand Reinhold, New York, pp. 85–100.

Zaragosi, S., Bourillet, J.F., Eynaud, F., Toucanne, S., Denhard, B., Van Toer, A., et al., 2006. The impact of the last European deglaciation on the deep-sea turbidite systems of the Celtic–Armorican margin (Bay of Biscay). Geo-Marine Letters 26, 317–329.

Ziegler, M., Jilbert, T., de Lange, G.J., Lourens, L.J., Reichart, G.J., 2008. Bromine counts from XRF scanning as an estimate of the marine organic carbon content of sediment cores. Geochemistry, Geophysics, Geosystems 9, 212–234.